**Key Points:**
- Budgets of moisture, momentum, and heat were computed to study the mechanism for the record-breaking rainfall in Guangzhou, China
- The persistent onshore warm and moist mesoscale flow from the south and east in the lower troposphere provided the main fuel
- Buoyancy and dynamic acceleration and the shallow weak cool pools jointly supported the sustained and strong slantwise updrafts

# Budget Analyses of a Record-Breaking Rainfall Event in the Coastal Metropolitan City of Guangzhou, China

**Yongjie Huang[1,3]** iD**, Yubao Liu[1,2]** iD**, Yuewei Liu[1], and Jason C. Knievel[1]**

[1]National Center for Atmospheric Research (NCAR), Boulder, CO, USA, [2]Precision Regional Earth Modeling and Information Center, Nanjing University of Information Science and Technology, Nanjing, China, [3]School of Meteorology, University of Oklahoma, Norman, OK, USA

**Abstract** To investigate the mechanisms for the record-breaking rainfall in the coastal metropolitan city of Guangzhou, China during 6–7 May 2017, budget analyses of advection and source/sink terms of the water vapor, potential temperature, and vertical momentum equations were conducted using the model output of a nested very large eddy simulation with the Weather Research and Forecasting model. Results show that the warm and moist air flows from the south and east onshore in the lower troposphere provided the main moisture source for the heavy rainfall. The structure of vertical velocity and hydrometeors (low-echo centroid structure), in which the heavy rainfall was separated from the low-level updraft, was favorable for the formation and maintenance of a heavy precipitation rate. The removal of the heat due to the advection (cooling tendency) in the upper troposphere increased the convective available potential energy of parcels rising from the lower troposphere, maintaining the development of updrafts. Although the total buoyancy forcing was the main contribution term for maintaining the updrafts, total dynamic acceleration played an important role in the vertical acceleration below the maximum vertical velocity core. In particular, the nonlinear dynamic perturbation pressure gradient force in the lower troposphere induced by the rotations aloft maintained the strong updrafts.

## 1. Introduction

Flash flooding associated with extreme rainfall gravely threatens life and property around the world, especially in urban areas (Huang, Liu, et al., 2019; Kermanshah et al., 2017; Sharif et al., 2006). In the last several decades, there have been great advancements in scientific understanding of the processes that drive heavy rainfall, in simulating it with numerical weather prediction models, and in forecasting it operationally. However, it is still a formidable challenge to predict the magnitude of extreme rainfall accurately, that is, through quantitative precipitation forecasting (Doswell et al., 1996; Fritsch & Carbone, 2004).

Heavy precipitation results from high rainfall rates with a prolonged duration. Doswell et al. (1996) developed an ingredients-based approach to forecasting the potential for flash flood-producing storms. Heavy rainfall hinge on strong ascent rate of air containing abundant moisture, high precipitation efficiency, and long duration of high rainfall rates. Phenomena that comprise these ingredients include quasi-stationary long-lived rainfall-producing systems (Doswell et al., 1996). From Doswell et al. (1996), the rainfall rate $R$ can be expressed simply as

$$R = Ewq,$$

wherein $E$ is the precipitation efficiency, which is a proportionality coefficient relating rainfall rate to input moisture flux; $w$ is the ascent rate; and $q$ is the water vapor mixing ratio of the rising air. Based on this equation, once the ascending moisture is present, the qualities of its thermodynamic environment that affect vertical motion are key for forecasting the severity of heavy precipitation.

Stevenson and Schumacher (2014) surveyed extreme rainfalls in the central and eastern United States over a 10-year period using gridded multisensor (radar and gauge) precipitation analyses and found that approximately 30% of extreme rainfalls in this period were associated with synoptic systems, and 7% with tropical cyclones, but 63% with mesoscale convective systems (MCSs). These findings are consistent with previous studies (Schumacher & Johnson, 2005, 2006). Most of the MCS cases were classified as training-line/adjoining-stratiform (TL/AS) or back-building/quasi-stationary (BB) types (Schumacher & Johnson, 2005;

Stevenson & Schumacher, 2014). TL/AS systems often form along an east-west oriented, preexisting slow-moving surface boundary, and embedded "training" convective cells move eastward (Peters & Schumacher, 2015; Schumacher & Johnson, 2005; Stevenson & Schumacher, 2014). In contrast, BB systems depend more on mesoscale and storm-scale forcing, especially cold pool outflows. In BB systems, new convective cells repeatedly form in the upstream regions of their predecessors and move over a particular area (Schumacher, 2015; Schumacher & Peters, 2017). Both types of MCSs can support sustained periods of rain and large rainfalls. However, Schumacher and Johnson (2005) indicated that the typical scale of BB MCSs is smaller and thus BB MCSs are less predictable than TL/AS MCSs. Many case studies that examine extreme-rainfall-producing MCSs in China also found similar MCS patterns of organization (e.g., Huang, Liu, et al., 2019; Luo et al., 2014; Luo & Chen, 2015; Wang et al., 2014; Zhang & Zhang, 2012).

Several studies showed that some BB MCSs with embedded mesoscale convective vortices or supercells can lead to extreme short-lived rainfall rates and high accumulations (Nielsen & Schumacher, 2018; Schumacher & Johnson, 2008, 2009; Smith et al., 2001). Nielsen and Schumacher (2018) conducted a series of numerical model simulations to investigate the role of in-storm rotations in supporting storm-scale updrafts associated with extreme rainfall. They found that intense, rotationally induced low-level dynamical accelerations associated with the nonlinear dynamic vertical perturbation pressure gradient force (VPPGF) can enhance low-level updrafts and support extreme rainfall rates.

The purpose of our paper is to focus on a record-breaking rainfall, with a daily maximum of 524.1 mm, that occurred over the coastal metropolitan city of Guangzhou, China, during 6–7 May 2017, causing serious floods and property damage. Huang, Liu, et al. (2019) conducted an observation analysis and a nested large-eddy simulation with Weather Research and Forecasting (WRF) model to examine the key environmental forcing factors that contributed to the extreme rainfall, including synoptic conditions, topographic effects, convective cold pools, and urban effects. They found that the sustained, strong, warm-moist southerly flow in the lower troposphere in the trumpet-shaped topography of the Pearl River Delta played a key role. The interaction between the relatively weak cold pool associated with evaporating precipitation and the warm-moist southerly flow supported the initiation and maintenance of a long-lived BB MCS, which delivered the record rainfall.

On 6 May 2017, a maximum hourly rainfall of 184.4 mm was recorded in Xintang Town, Zengcheng (ZC) District. The reason for this extreme value is unclear. It is of great interest to understand the internal thermodynamic and dynamic processes of the storm that supported the updrafts and high rainfall rates. For this study we performed budget analyses to shed light on the moisture and heat balance, and thermodynamic and dynamic processes in the MCS. The rest of the paper is organized as follows. Section 2 describes the record-breaking rainfall event and numerical simulation design. The analysis methods used in this study are given in section 3. Results are presented in section 4. Section 5 gives the summary and conclusions of the study.

## 2. Event Description and Numerical Simulation

Torrential rainfall occurred in the metropolitan city of Guangzhou, southern China, during 6–7 May 2017, causing serious floods and property damage. A maximum daily rainfall of 524.1 mm was recorded at Jiulong Town, Huangpu (HP) District of Guangzhou, which broke the previous maximum daily rainfall record 477.4 mm at Paitan Town of Guangzhou on 23 May 2014. A maximum hourly rainfall of 184.4 mm was recorded in Xintang Town, ZC District, which was just short of the maximum hourly rainfall record of Guangdong Province (188.0 mm at Baisha Town of Yangjiang on 23 June 2013).

In this study, output from the same WRF nested very large-eddy simulation as described in Huang, Liu, et al. (2019) is used for budget analyses. The model was integrated with three nested domains with horizontal grid spacings of 4.5, 1.5, and 0.5 km, respectively. The large-eddy simulation mode was set up in the 0.5-km domain with no PBL parameterization. The real-time four-dimensional data assimilation and forecasting system, developed at Research Application Laboratory of National Center for Atmospheric Research (Huang et al., 2018; Liu et al., 2008; Liu et al., 2008), was used to assimilate surface observations, soundings, and wind-profiler data. Comparing the model output with global reanalyses and observations from automatic weather stations, rain gauges, and Doppler radar confirmed that the model simulation reproduced
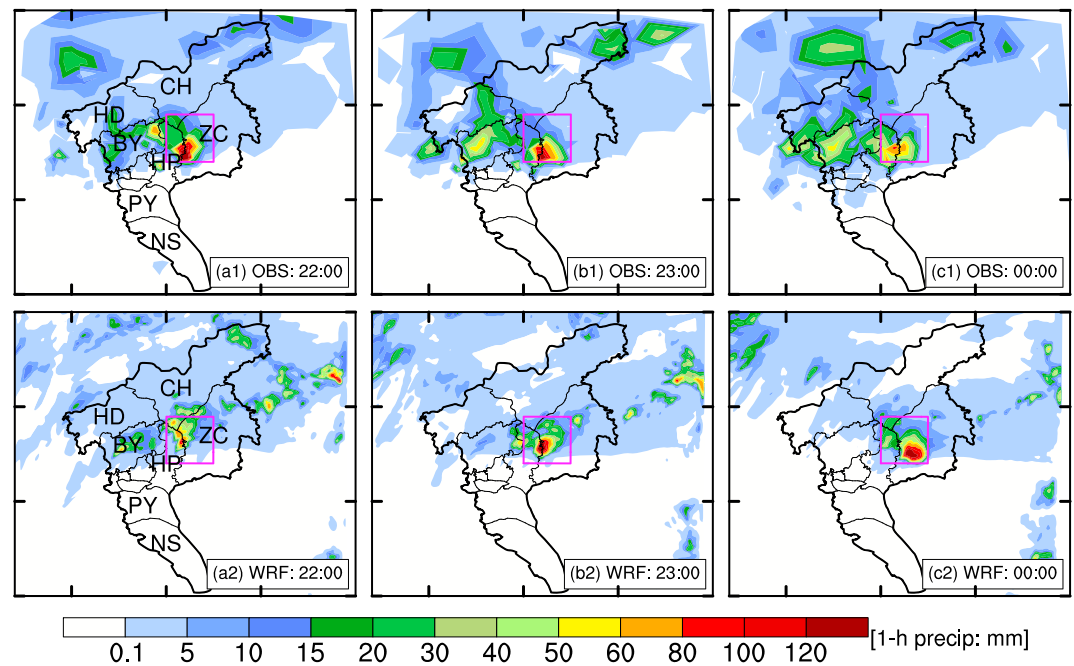
**Figure 1.** (a1–c1) Observed and (a2–c2) simulated 1-hr accumulated precipitation (mm) over Guangzhou from 2200 UTC 6 to 0000 UTC 7 May 2017 at 1-hr intervals. The magenta boxes indicate the region for calculating moisture flux in Figure 2. The thick and thin solid black lines represent Guangzhou City and its district borders, respectively. Tick marks are included every 50 km. The initials in (a1) and (a2) are as follows: HD = Huadu District; CH = Conghua District; BY = Baiyun District; HP = Huangpu District; ZC = Zengcheng District; PY = Panyu District; and NS = Nansha District.

the initiation and development of the moist convection and heavy rainfall generally well. Please refer to the paper by Huang, Liu, et al. (2019) for more details of the model configuration and verification.

Figure 1 shows observed and simulated hourly accumulated precipitation in Guangzhou city from 2200 UTC 6 to 0000 UTC 7 May 2017. Very intense and concentrated precipitation occurred in the region between HP and ZC. The model captured the observed hourly accumulated precipitation intensity (simulated maximum is 155.6 mm at 2300 UTC 6 May; Figure 1b2) and spatial distribution (Figure 1). The main purpose of these budget analyses in this study is to understand the development mechanism for this intense rainfall. The rainstorm presented steady dynamical features during this period. In this paper, 1-hr (2200–2300 UTC 6 May 2017) simulated data were selected for the budget analyses.

## 3. Method

Moisture and cooling, typically from rising air, are two necessary factors for heavy rainfall. Therefore, moisture flux is used to examine the main moisture source for heavy rainfall, and budgets of vertical momentum, thermodynamics, and vertical vorticity are used to investigate how buoyancy forcing and dynamic forcing support the strong updrafts.

### 3.1. Moisture Flux

In order to quantitatively estimate the moisture source of the heavy rainfall, the moisture flux across the four boundaries of a rectangular region enclosing the main heavy rainfall area (Figure 1) was calculated using the following equation:

$$QFlux_x = \int_0^{L_x} Q_v V_n dls, x \in (W, E, S, N) \tag{1}$$

wherein $QFlux_x$ is moisture flux across boundary x and x can be one of the W (west), E (east), S (south), or N (north) boundaries to the region. On the right side of equation (1), $Q_v$, $V_n$, and $L_x$ are water vapor mixing ratio, wind vector component normal to boundary x (inward direction is positive, and outward direction is negative), and the length of boundary x, respectively.

### 3.2. Potential Temperature Equation

The heat budget of the system was computed based on the potential temperature equation of the WRF model. Each term of the equation was output during the WRF run, and then used to compute the heat budgets, shown in the following simplified thermal equation,

$$\underbrace{\frac{\partial \theta}{\partial t}}_{\text{TH\_TEND}} = \underbrace{-\vec{V}_h \cdot \nabla_h \theta}_{\text{TH\_ADVH}} \underbrace{-w\frac{\partial \theta}{\partial z}}_{\text{TH\_ADVZ}} + \underbrace{\frac{\partial \theta}{\partial t}\Big|_{\text{MP}}}_{\text{TH\_MP}} + \frac{\partial \theta}{\partial t}\Big|_{\text{RES}}, \tag{2}$$

wherein the term $\frac{\partial \theta}{\partial t}$ on the left side of equation (2) is total potential temperature tendency (hereafter TH_TEND) and the terms on the right side of equation (2) are potential temperature tendencies due to horizontal advection ($-\vec{V}_h \cdot \nabla \theta$, hereafter TH_ADVH), vertical advection ($-w\frac{\partial \theta}{\partial z}$, hereafter TH_ADVZ), microphysical latent heating ($\frac{\partial \theta}{\partial t}_{\text{MP}}$, hereafter TH_MP), and the residual term ($\frac{\partial \theta}{\partial t}_{\text{RES}}$, including radiative heating and diffusion). We found the residual term ($\frac{\partial \theta}{\partial t}_{\text{RES}}$) was relatively smaller than the other terms in equation (2) in this study (not shown). Therefore, we did not discuss this term for the purposes of this study.

### 3.3. Vertical Momentum Budgets and Perturbation Pressure Decomposition

The terms of the WRF model's vertical momentum prognostic equation were output to investigate the vertical momentum budget responsible for the heavy rainfall. The vertical momentum prognostic equation can be expressed as

$$\underbrace{\frac{\partial w}{\partial t}}_{\text{W\_TEND}} = \underbrace{-\vec{V}_3 \cdot \nabla_3 w}_{\text{W\_ADV}} \underbrace{-\frac{1}{\rho_0}\frac{\partial p'}{\partial z}}_{\text{VPPGF}} + B + \frac{\partial w}{\partial t}\Big|_{\text{RES}}, \tag{3}$$

wherein the total vertical momentum tendency ($\frac{\partial w}{\partial t}$, hereafter W_TEND) is the sum of vertical acceleration resulting from advection ($-\vec{V}_3 \cdot \nabla_3 w$, hereafter W_ADV), VPPGF ($-\frac{1}{\rho_0}\frac{\partial p'}{\partial z}$), thermal buoyancy ($B$), and other acceleration ($\frac{\partial w}{\partial t}_{\text{RES}}$, e.g., Coriolis, curvature, and diffusion terms). It is found that the residual term ($\frac{\partial w}{\partial t}_{\text{RES}}$) was 1 order of magnitude smaller than the other terms in equation (3) in this study (not shown). Therefore, we neglected this term for the purposes of this study. The thermal buoyancy $B$ is expressed as

$$B = g\left(\frac{\theta'}{\theta_0} + 0.61q_v' - q_H\right), \tag{4}$$

wherein $\theta'$ and $\theta_0$ are the perturbation and background potential temperature, respectively; $q_v'$ is the perturbation water vapor mixing ratio; and $q_H = Q_c + Q_i + Q_r + Q_s + Q_g$, wherein $Q_c$, $Q_i$, $Q_r$, $Q_s$, and $Q_g$ are mixing ratios of cloud water, cloud ice, rain water, snow, and graupel, respectively.

The perturbation pressure in equation (3) can be decomposed into the dynamical and buoyant components as $p' = p_D' + p_B'$ following Rotunno and Klemp (1982) and Klemp (1987). The diagnostic pressure equations based on the anelastic approximation and the absence of friction (Parker & Johnson, 2004; Rotunno & Klemp, 1982; Weisman & Rotunno, 2000) are

$$\nabla^2 p_B' = \frac{\partial}{\partial z}(\rho_0 B) \tag{5}$$

and

$$\nabla^2 p_D' = -\rho_0\left[\left(\frac{\partial u}{\partial x}\right)^2 + \left(\frac{\partial v}{\partial y}\right)^2 + \left(\frac{\partial w}{\partial z}\right)^2 - w^2\frac{\partial^2}{\partial z^2}(ln\rho_0)\right] - 2\rho_0\left(\frac{\partial v}{\partial x}\frac{\partial u}{\partial y} + \frac{\partial u}{\partial z}\frac{\partial w}{\partial x} + \frac{\partial v}{\partial z}\frac{\partial w}{\partial y}\right) \tag{6}$$

By separating the velocities into mean and perturbation components, the linear component of equation (6) can be obtained

$$\nabla^2 p'_{\text{DL}} = -2\rho_0 \left( \frac{\partial u_0}{\partial z} \frac{\partial w}{\partial x} + \frac{\partial v_0}{\partial z} \frac{\partial w}{\partial y} \right), \tag{7}$$

and the residual component is the nonlinear part. To interpret these components physically, Davies-Jones (2002) decomposed the nonlinear term as "splat" (the sum of the fluid extension and shear terms involving deformation) and "spin" terms, which are physically meaningful and invariant to three-dimensional rotations of the coordinate axes. Due to $\nabla^2 p' \propto -p'$ and following Markowski and Richardson (2010), for well-behaved, incompressible, storm-scale flows, perturbation pressure $p'$ is approximately written as

$$p' \propto \underbrace{\underbrace{e'_{ij}}_{\text{splat}} \underbrace{-\frac{1}{2}|\vec{\omega}'|^2}_{\text{spin}}}_{\text{Nonlinear dynamic } p' \ (p'_{\text{DNL}})} + \underbrace{2\vec{S}\cdot\nabla_h w'}_{\text{Linear dynamic } p' \ (p'_{\text{DL}})} \underbrace{-\frac{\partial B}{\partial z}}_{\text{Buoyancy } p' \ (p'_{\text{B}})}, \tag{8}$$

wherein $e'_{ij}$ is the deformation perturbation, $\vec{\omega}'$ is total vorticity perturbation, $\vec{S} = (\partial u_0/\partial z, \partial v_0/\partial z)$ is the mean vertical environmental wind shear, and $\nabla_h w' = (\partial w'/\partial x, \partial w'/\partial y)$ is the horizontal gradient of the vertical velocity perturbation. In the nonlinear dynamic perturbation pressure term (the first two terms on the right-hand side), the splat term due to deformation is always associated with positive perturbation pressure, while the spin term due to rotation (cyclonic or anticyclonic in any direction) is always associated with negative perturbation pressure. The linear dynamic perturbation pressure term (the third term on the right-hand side) is associated with an updraft interacting with the ambient vertical wind shear. From (8), relatively low perturbation pressure is found on the downshear side of a localized updraft, and high perturbation pressure on the upshear side.

Numerically, $p'_B$, $p'_D$ and $p'_{DL}$ can be diagnosed by solving the three-dimensional Poisson equations (5)–(7) with appropriate boundary conditions (Coffer & Parker, 2015; Wang et al., 2016). Then the nonlinear dynamic perturbation pressure $p'_{DNL}$ can be obtained as the residual $p'_{DNL} = p'_D - p'_{DL}$. We used the same boundary conditions and method as in Coffer and Parker (2015) to solve these Poisson equations. Please refer to Coffer and Parker (2015) for the detailed description. Therefore, the total dynamic acceleration (hereafter ACCD) is induced by the linear ($-\frac{1}{\rho_0}\frac{\partial p'_{DL}}{\partial z}$, hereafter LD_VPPGF) and nonlinear dynamic ($-\frac{1}{\rho_0}\frac{\partial p'_{DNL}}{\partial z}$, hereafter NLD_VPPGF) pressure perturbation gradient force. The total buoyancy acceleration (hereafter ACCB) contains both thermal buoyancy $B$ and perturbation pressure gradient force driven by buoyancy perturbation, that is, ACCB $= B - \frac{1}{\rho_0}\frac{\partial p'_B}{\partial z}$, referred to as the buoyancy forcing, which is independent of the somewhat arbitrary choice of the base state, unlike $B$ and $-\frac{1}{\rho_0}\frac{\partial p'_B}{\partial z}$ (Doswell & Markowski, 2004).

### 3.4. Vorticity Equation

Because of the contribution of the rotation in the nonlinear dynamic forcing, a vorticity equation is used to diagnose vorticity-generation rates. The vertical vorticity equation in Cartesian coordinates is expressed as

$$\frac{\partial \zeta}{\partial t} = \underbrace{-\left( u\frac{\partial \zeta}{\partial x} + v\frac{\partial \zeta}{\partial y} \right)}_{\text{Horizontal advection}} \underbrace{-w\frac{\partial \zeta}{\partial z}}_{\text{Vertical advection}} + \underbrace{\left( \frac{\partial w}{\partial y}\frac{\partial u}{\partial z} - \frac{\partial w}{\partial x}\frac{\partial v}{\partial z} \right)}_{\text{Tilting}} \underbrace{-(\zeta + f)\left( \frac{\partial u}{\partial x} + \frac{\partial v}{\partial y} \right)}_{\text{Stretching/divergence}}$$
$$+ \underbrace{\frac{1}{\rho^2}\left( \frac{\partial \rho}{\partial x}\frac{\partial p}{\partial y} - \frac{\partial \rho}{\partial y}\frac{\partial p}{\partial x} \right)}_{\text{Solenoid}} \underbrace{-v\frac{\partial f}{\partial y}}_{\text{Coriolis}} + \frac{\partial \zeta}{\partial t}_{\text{RES}}, \tag{9}$$

wherein $\zeta$ is the vertical component of the relative vorticity, $f$ is the Coriolis parameter, and $\rho$ and $p$ are the air density and pressure, respectively. The terms on the right side of equation (9) are the vorticity horizontal advection, vorticity vertical advection, tilting term (representing the tilting of horizontal vorticity into the vertical), stretching (or divergence) term, solenoid term, Coriolis advection (the change in vertical vorticity resulting from latitudinal displacement), and the residual term (e.g., friction and diffusion).

## 4. Results

### 4.1. Moisture Source

Figure 2 shows time-height cross sections of moisture flux across four boundaries ($QFlux_W$, $QFlux_E$, $QFlux_S$, and $QFlux_N$) depicted in magenta in Figure 1. The net zonal and meridional moisture fluxes and total moisture flux are also displayed in Figure 2. There were strong inward moisture fluxes across the eastern (positive $QFlux_E$) and southern (positive $QFlux_S$) boundaries in the lower troposphere, mainly below 4 km, with maxima over 1,800 kg·kg$^{-1}$ m$^2$·s$^{-1}$ (Figures 2b and 2d). The strong inward moisture flux across the western boundary (positive $QFlux_W$) in the upper troposphere (Figure 2a) was mostly canceled by the strong outward moisture flux at the eastern boundary (negative $QFlux_E$) in the upper troposphere (Figure 2b). This mainly resulted from the prevailing westerly flows in the upper troposphere (Huang, Liu, et al., 2019). The positive net zonal moisture flux was concentrated in the lower troposphere, and the maximum reached 2,250 kg·kg$^{-1}$ m$^2$·s$^{-1}$ (Figure 2c). In the meridional direction, the net inward moisture flux was mainly below 2 km, and the maximum reached 2,250 kg·kg$^{-1}$ m$^2$·s$^{-1}$ (Figure 2f), resulting from strong inward moisture flux across the southern boundary and weak inward/outward moisture fluxes across the northern boundary (Figures 2d and 2e).

Based on the total moisture flux and the average precipitation and precipitable water rates shown in Figure 2 g, we conclude that the main moisture source for the heavy precipitation in this region was the lower troposphere, from the south and east. The moisture flux vectors ($Q_vu$ and $Q_vv$) at 500 m (Figure 2h) are consistent with this conclusion. From Figure 2g, the variation of precipitation rate is delayed slightly compared to the precipitable water rate, indicating incoming water vapor quickly transforms into precipitation, and indirectly reflecting the high precipitation efficiency during this period. The ratio of accumulated moisture fluxes below 4 km across different boundaries to the total moisture flux below 4 km are 31.2% for the western boundary, 17.9% for the eastern boundary, −30.3% for the northern boundary, and 81.2% for the southern boundary. Therefore, the moist southerly flow in the lower troposphere emphasized by Huang, Liu, et al. (2019) was very important for this heavy rainfall, which supplied abundant water vapor to the precipitation region.

### 4.2. Overall Structures of the Storm

Figure 3a shows 1-hr accumulated precipitation and time-averaged vertical velocity at 2 km above mean sea level from 2200 to 2300 UTC 6 May 2017. Very intense precipitation (>150 mm/hr) was produced over the district boundary between HP and ZC. In this study, model output data at 1-min intervals were used to calculate the time average. The strong updraft was mainly located to the southwest of the heavy rainfall core behind the cold pool periphery, and the downdraft was located on the northeastern side. To study the vertical structure of the rainstorm, vertical cross sections are created along the black thick line through the maximum-accumulated-precipitation core shown in Figure 3a. Vertical cross sections of time-averaged (2200–2300 UTC 6 May 2017) vertical velocity, cloud water mixing ratio, rain water mixing ratio, sum of cloud ice and snow mixing ratios, and graupel mixing ratio are shown in Figure 3b. Strong vertical motion (maximum 1-hr averaged vertical velocity reaching 5.7 m/s) existed from the lower to upper troposphere, slightly offset southwestward from the maximum-accumulated-precipitation core. With abundant moisture in the lower troposphere (Figure 2), strong vertical moisture flux ($wq$) supported a high precipitation rate (Doswell et al., 1996). There was relatively weak vertical upward motion in the lower troposphere (mainly below 4 km) to the southwest of the maximum-accumulated-precipitation core, where shallow cloud developed (cloud water mixing ratio shown in Figure 3b) and new cells formed (discussed below). There was a downdraft below 3 km on the northeastern side of the maximum-accumulated-precipitation core. The distribution of cloud water coincided with the ascending areas (Figure 3b). Large amounts of rain water and graupel existed over the maximum-accumulated-precipitation core (with high rainfall rate). Radar reflectivity >50 dBZ developed below the 0 °C layer (Figure 3b), defining a low-echo centroid structure and indicating the importance of warm-rain processes (Smith et al., 2000; Vitale & Ryan, 2013). The low-echo centroid structure is characteristic of numerous storms that cause catastrophic flash floods (Hamada et al., 2015; Smith et al., 2000). Warm-rain processes are typically more efficient than cold-rain processes (Lamb, 2001). Precipitation efficiency was calculated by using the definition of Doswell et al. (1996), that is, the ratio of water mass falling as precipitation versus the influx of water vapor mass into the cloud. The precipitation efficiency values were 86.5% and 92.8% in the periods of 2200–2300 UTC 6 May and 2100 UTC 06–0000 UTC
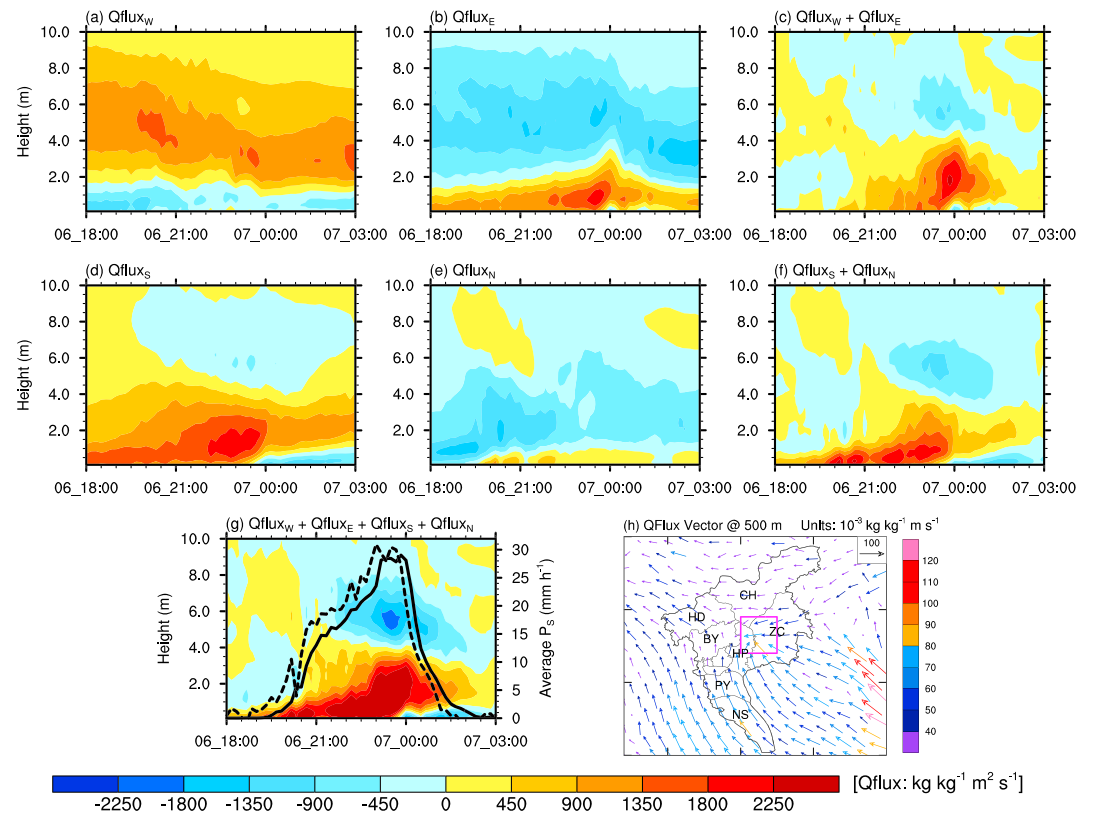
**Figure 2.** Time-height cross sections of moisture fluxes (kg·kg$^{-1}$ m$^2$·s$^{-1}$) across (a) west ($QFlux_W$), (b) east ($QFlux_E$), (d) south ($QFlux_S$), and (e) north ($QFlux_N$) boundaries of the magenta boxes shown in Figure 1 and (c) zonal ($QFlux_W$ + $QFlux_E$), (f) meridional ($QFlux_S$ + $QFlux_N$) net moisture fluxes, and (g) total moisture flux ($QFlux_W$ + $QFlux_E$ + $QFlux_S$ + $QFlux_N$) from 1800 UTC 6 to 0300 UTC 7 May 2017. The black thick solid and dashed curves in (g) are average precipitation rate (mm/hr) within the box and precipitable water rate (mm/hr) within the box from the total moisture flux, respectively. Time-averaged moisture flux vectors (units: 10$^{-3}$ kg·kg$^{-1}$ m·s$^{-1}$) at 500 m above mean sea level during 2200–2300 UTC 6 May 2017 are shown in (h). Arrows in (h) are color coded according to the magnitude of the moisture flux. Tick marks in (h) are included every 50 km.

7 May 2017, respectively, which are much higher than those of general storms in previous studies (most are less than 50%; Market et al., 2003). The northeastward mean cloud-layer wind (Figure 3a) and wind-shear-caused (Figure 3b) moderately backward slanting convective updrafts allowed heavy rainfall to shift behind the low-level updraft, which favored development of the sustained updrafts and heavy rainfall.

### 4.3. Vertical Momentum Budget

The vertical cross sections of vertical velocity from 2150 to 2300 UTC 6 May 2017 at 10-min intervals are shown in Figure 4. At 2150 UTC (Figure 4a), there was a mature convective cell A1 over the core of maximum accumulated precipitation. Meanwhile, a new convective cell A2 was developing to the southwest of convective cell A1. Cell A2 continued developing with time and finally merged with cell A1 to form a large combined cell (A1 + A2) at 2220 UTC 6 May 2017 (Figure 4d). Thereafter, cell A1 + A2 moved southeastward away from the location of the cross section, so that the cell does not appear in Figure 4e. However, a new convective cell B was generated to the southwest of the core of maximum accumulated precipitation (Figure 4e). Then cell B strengthened and moved northeastward (Figures 4f–4h). To study the forcing mechanism for the updrafts in the front and above the core of maximum accumulated precipitation, we analyzed a vertical momentum budget.

In order not to mix up the dynamics of different convective cells A1 + A2 and B, the cell depicted in Figures 4c and 4d was selected for study. Figure 5 shows time-averaged (2210–2220 UTC 6 May 2017) total vertical velocity tendency and the main terms of the vertical momentum equation, including advection,
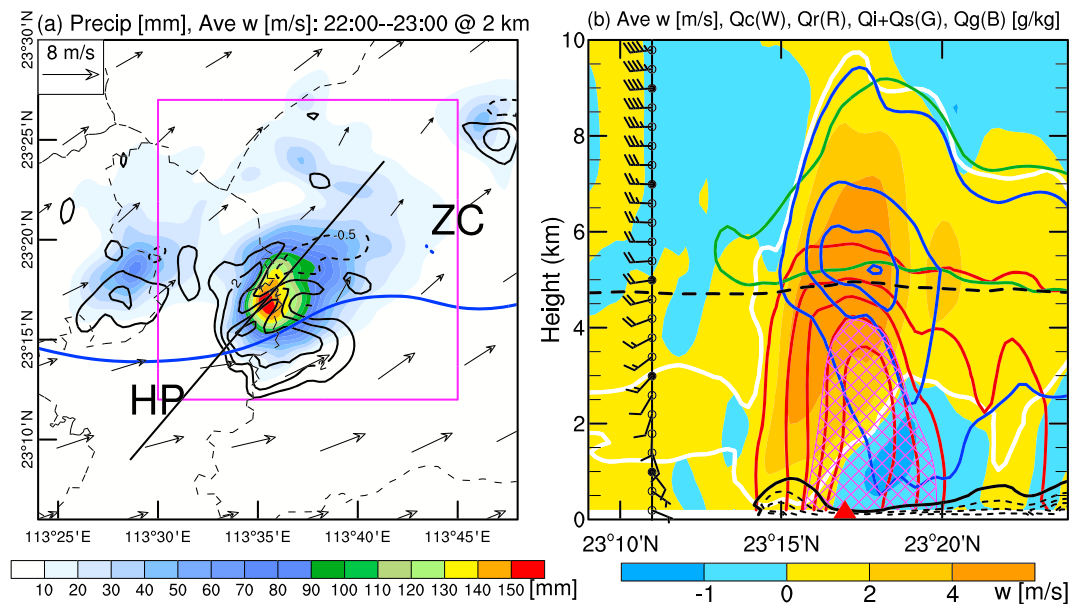
**Figure 3.** (a) Accumulated precipitation (shaded, mm), time-averaged vertical velocity (black contours: −0.5, 1, 2, 3, and 4 m/s; dashed contours are used for negative values) at 2 km above mean sea level, and time-averaged cloud-layer wind vectors (average of 850-, 700-, and 500-hPa wind vectors in m/s) from 2200 to 2300 UTC 6 May 2017. The blue thick contour in (a) shows the 0-K perturbation temperature at 300 m above mean sea level indicating cold pool periphery. The magenta box is the same as those in Figures 1 and 2h. The thin black dashed lines in (a) represent the district borders in Guangzhou. (b) Vertical cross sections along the black thick solid line in (a) of time-averaged vertical velocity (color shaded, m/s), cloud water mixing ratio (white contour: 0.1 g/kg), rain water mixing ratio (red contours: 0.1, 1, 2, 3, and 4 g/kg), sum of cloud ice and snow mixing ratio (green contour: 0.1 g/kg), and graupel mixing ratio (blue contours: 0.1, 1, 2 and 3 g/kg) from 2200 to 2300 UTC 6 May 2017. The black dashed line in (b) indicates 0 °C isotherm, and the magenta cross-hatched pattern represents the area with radar reflectivity over 50 dBZ. The black contours near the surface in (b) show perturbation temperature (−1.2, −0.8, −0.4, and 0 K; dashed contours are used for negative values). The wind profile in (b) indicates spatiotemporal-averaged horizontal winds at 400-m intervals (one full wind barb represents 4 m/s). The red triangle in (b) represents the location of maximum-accumulated-precipitation core.

vertical pressure gradient force, and buoyancy. Here, we first examine the sum of the vertical pressure gradient force and buoyancy and then analyze the individual contributions of the buoyancy and dynamic acceleration.

In the horizontal cross sections at 1 km above mean sea level, negative vertical velocity tendency exists near the core of maximum accumulated precipitation (Figure 5a). However, its value is an order of magnitude smaller than those of the advection term (Figure 5b) and the vertical pressure gradient force and buoyancy term (Figure 5c). There was positive vertical velocity tendency at 1 km to the south and southwest of the maximum-accumulated-precipitation core (Figure 5a), consistent with the convective development in this region. There was strong vertical pressure gradient force and buoyancy acceleration at 1 km to the south and southwest of the core of maximum accumulated precipitation (Figure 5c), while there was deceleration due to advection in this region (Figure 5b). The vertical velocity tendency in the upper level (at 5.4 km, Figures 5d–5f) shows strong vertical acceleration near the core of maximum accumulated precipitation (Figure 5d), which was apparently attributed to advection component (Figure 5e). The vertical pressure gradient force and buoyancy acceleration occurred in this region also (Figure 5f). The vertical cross sections (Figures 5g–5i) show that the strong vertical pressure gradient force and buoyancy acceleration were mainly in the lower troposphere below 6 km, especially below the maximum vertical velocity center (Figure 5i), supporting the development of vertical motion (Figure 5g). The advection term mainly transported the vertical velocity from the lower to the upper troposphere. The advection formed a region with negative vertical velocity tendency immediately below the maximum vertical velocity center and a positive right above the maximum vertical velocity center (Figure 5h). The vertical pressure gradient force and buoyancy acceleration upstream of the heavy rain core were the main forces maintaining the storm updrafts.
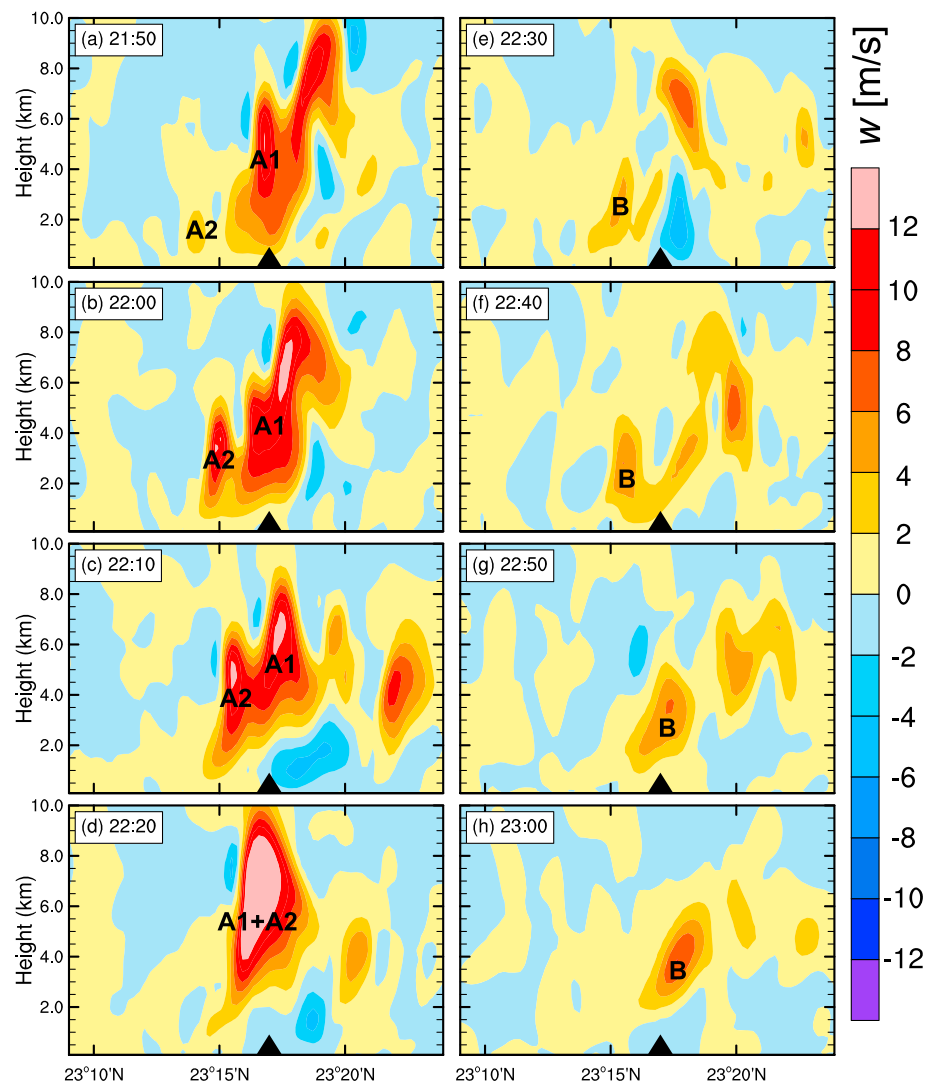
**Figure 4.** Vertical cross sections along the black thick solid line in Figure 3a of vertical velocity (m/s) from 2150 to 2300 UTC 6 May 2017 at 10-min intervals (a–h). The black triangles represent the location of maximum accumulated precipitation from 2200 to 2300 UTC 6 May 2017. The marks "A1," "A2," and "B" indicate different convective cells.

To further analyze the dynamics of the storm, the combined vertical pressure gradient force and buoyancy term were decomposed into total dynamic acceleration (ACCD) and total buoyancy acceleration (ACCB) by using the method introduced in section 3.3. The ACCD was further decomposed into the linear dynamic perturbation pressure gradient force (LD_VPPGF) and the nonlinear dynamic perturbation pressure gradient force (NLD_VPPGF). Figure 6 shows the vertical cross sections of time-averaged (2210–2220 UTC 6 May 2017) ACCB, ACCD, LD_VPPGF, and NLD_VPPGF. The ACCB was the main force for supporting the development and maintenance of updrafts, corresponding to the warm anomaly areas of perturbation potential temperature (Figure 6a). This result is consistent with that of Huang, Liu, et al. (2019), who showed that high convective available potential energy (CAPE) was persistently observed in this region. The existence of abundant moisture in the lower troposphere (mentioned in section 4.1) and the latent heat removed in the upper troposphere (discussed in section 4.4) were important to maintain the total buoyancy. On the other hand, ACCD also played a role in the vertical velocity acceleration (Figure 6b), especially the NLD_VPPGF component in the lower troposphere on the southwest of the core of maximum accumulated precipitation (Figure 6d). LD_VPPGF accelerated the updrafts mainly in the middle troposphere on the left flank of the maximum vertical velocity core (Figure 6c). The mean horizontal winds increased clockwise
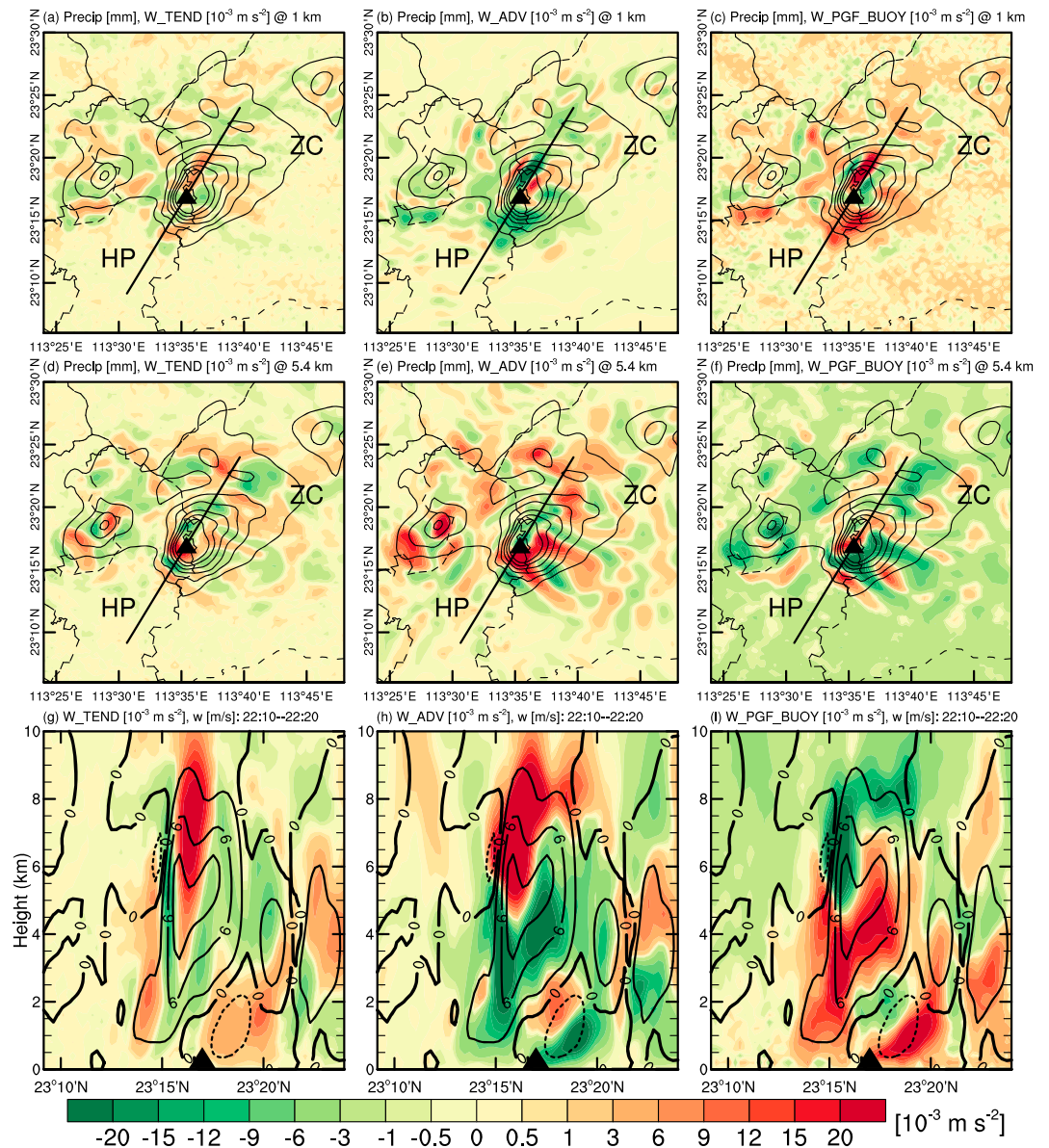
**Figure 5.** Time-averaged (2210–2220 UTC 6 May 2017) vertical velocity tendency (shaded, $10^{-3}$ m/s$^2$) at 1 and 5.4 km above mean sea level due to (a and d) total, (b and e) advection, and (c and f) vertical pressure gradient force and buoyancy and (g–i) corresponding vertical cross sections along the black thick solid lines in (a)–(c). The contours in (a)–(f) show the accumulated precipitation from 2200 to 2300 UTC 6 May 2017 (contours: 10, 30, 50, 70, 90, and 110 mm). The contours in (g)–(i) indicate the time-averaged vertical velocity (–2, 0, 2, 6, and 10 m/s; dashed contours are used for negative values). The thin black dashed lines in (a)–(f) represent the district borders in Guangzhou. The black triangles in all panels mark the location of maximum accumulated precipitation from 2200 to 2300 UTC 6 May 2017.

with increasing height (Figure 6c) indicating the mean vertical wind shear mainly pointed toward the right (east). From Figure 6c, positive $2\overrightarrow{S} \cdot \nabla_{\mathrm{h}} w'$ can be found on the upshear flank of the updraft (negative on the downshear flank) below the maximum vertical velocity core, associated with the distribution of high perturbation pressure based on equation (8). Therefore, the high perturbation pressure induced upward LD_VPPGF ($-\frac{1}{\rho_0}\frac{\partial p'_{\mathrm{DL}}}{\partial z}$) aloft on the upshear flank of the updraft (Figure 6c). In Figure 6d, the strongest vertical vorticity can be found at midlevels near the maximum vertical velocity core, so low perturbation pressure is associated at midlevels with the spin term in equation (8). Thus, upward-directed NLD_VPPGF ($-\frac{1}{\rho_0}\frac{\partial p'_{\mathrm{DNL}}}{\partial z}$) was found at lower levels below the altitude of the strongest vertical vorticity and
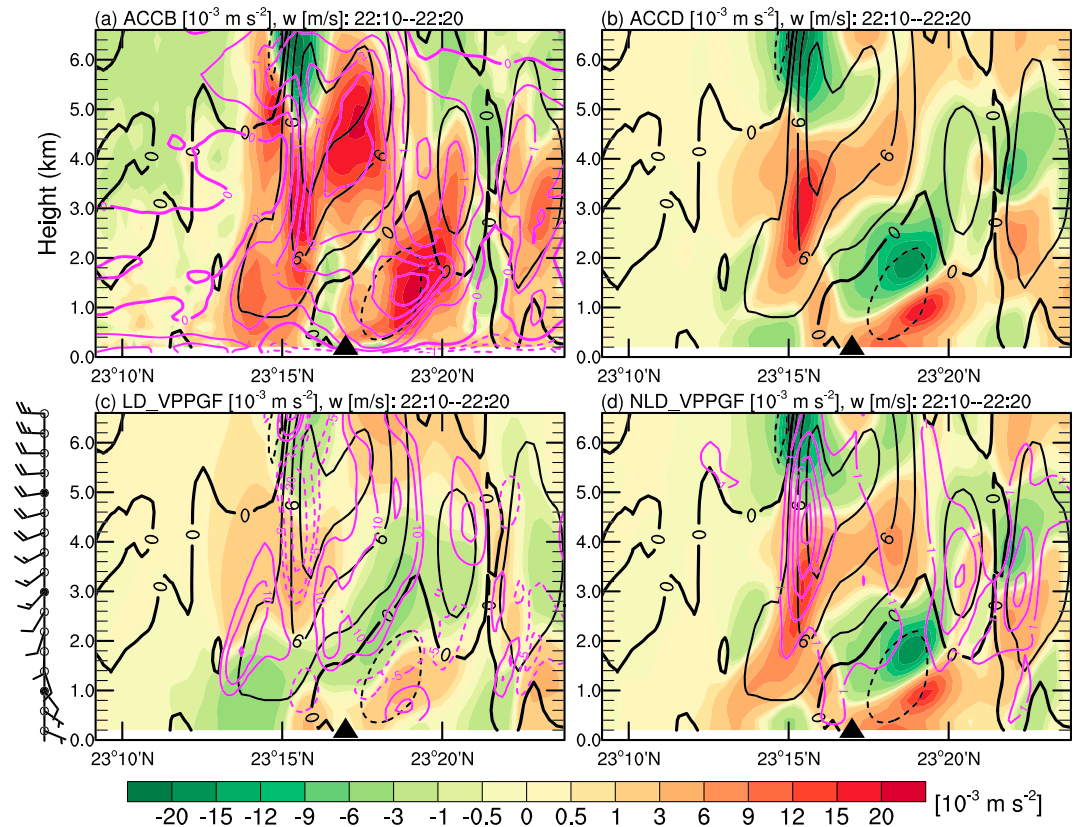
**Figure 6.** Vertical cross sections along the black thick solid line in Figure 5a of time-averaged (2210–2220 UTC 6 May 2017) (a) total buoyancy acceleration (ACCB, shaded, $10^{-3}$ m/s$^2$), (b) total dynamic acceleration (ACCD, shaded), (c) linear (LD_VPPGF), and (d) nonlinear (NLD_VPPGF) dynamic vertical perturbation pressure gradient acceleration (shaded). The black contours in each panel indicate the time-averaged vertical velocity (–2, 0, 2, 6, and 10 m/s; dashed contours are used for negative values). The magenta contours in (a), (c), and (d) indicate the time-averaged perturbation potential temperature (dashed contours are used for negative values, units: K), $2\overrightarrow{S} \cdot \nabla_h w'$ (–20, –10, –5, 5, 10, and $20 \times 10^{-6}$ s$^{-2}$; dashed contours are used for negative values) and vertical vorticity (1, 3, 5, 7, and $9 \times 10^{-3}$ s$^{-1}$), respectively. The wind profile on the left of (c) indicates spatiotemporal-averaged horizontal winds at 400-m intervals (one full wind barb represents 4 m/s). The black triangles represent the location of maximum accumulated precipitation from 2200 to 2300 UTC 6 May 2017.

supported the development of the updrafts. In brief, both buoyancy forcing and dynamic perturbation pressure acceleration (especially the nonlinear component associated with rotations) played important roles in supporting development and maintenance of updrafts. The same conclusions can be obtained from other time-averaged results, for example, 1-hr (2200–2300 UTC 6 May 2017) average (not shown).

### 4.4. Thermodynamic and Vertical Vorticity Budgets

Figure 7 displays the vertical cross sections of the time-averaged (2210–2220 UTC 6 May 2017) total potential temperature tendency, and the potential temperature tendencies due to microphysical latent heating, horizontal advection, and vertical advection, respectively. The perturbation potential temperature is also plotted in Figure 7. Several important conclusions can be drawn from the figure. First, a warm anomaly was collocated with the core of maximum accumulated precipitation core and with the area of microphysical latent heat release (Figure 7b), suggesting the latter was responsible for the anomaly and the buoyancy acceleration, especially to the upper-level updrafts. The latent heating here was mainly associated with water vapor condensation in the ascending regions, and the latent cooling was mainly associated with rain water evaporation in the descending regions (not shown; Huang et al., 2019). The second conclusion is that vertical advection played a key role in removing the latent heat released by the microphysical processes (Figure 7d), and horizontal advection also reduced some of the warm anomaly (Figure 7c). Both positive
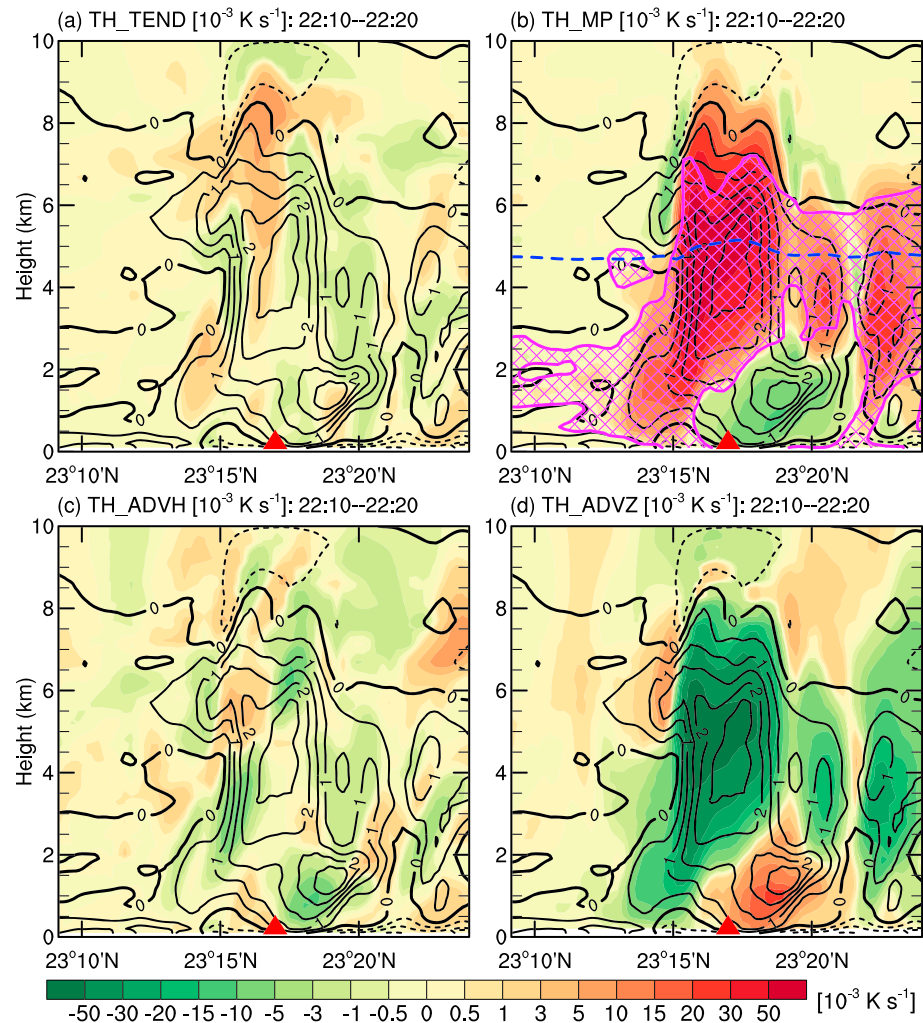
**Figure 7.** Vertical cross sections along the black thick solid line in Figure 5a of time-averaged (2210–2220 UTC 6 May 2017) (a) total potential temperature tendency, potential temperature tendencies due to (b) microphysical processes, (c) horizontal advection, and (d) vertical advection (shaded, $10^{-3}$ K/s). The contours in each panel show the perturbation potential temperature (dashed contours are used for negative values, units: K). The magenta cross-hatched pattern in (b) indicates the area with relative humidity over 99%, and the blue dashed lines indicate 0 °C isotherm. The red triangles represent the location of maximum accumulated precipitation from 2200 to 2300 UTC 6 May 2017.

and negative total potential temperature tendencies existed in the warm anomaly (Figure 7a), but their values were an order of magnitude smaller than those of latent heating and advection cooling. Therefore, the cooling from advection in the upper troposphere helped maintain the CAPE of the rising parcels that originated in the lower troposphere, which is consistent with the large CAPE generation rate attributable to the large-scale advection shown by Huang, Liu, et al. (2019). This process was crucial for the persistent development of updrafts. The third conclusion is that there was a cold anomaly near the surface layer, associated with the precipitation-induced cold pool. In the downdraft region, there was a moderate cooling core due to evaporative cooling (Figure 7b). It is important to point out that due to the northeastward mean cloud-layer winds (Figure 3a), the cold pool extended far downstream (northeast, Figures 3 and 7), which was helpful for maintaining the long-lasting slantwise updrafts. The fourth conclusion is that the relative humidity in the cold anomaly region was high (magenta cross-hatched pattern in Figure 7b) and there was latent heating in the low-level updraft region on the southwest flank of core of maximum accumulated precipitation (Figure 7b), which supplied high-energy (warm and moist) parcels to the main storm updrafts.
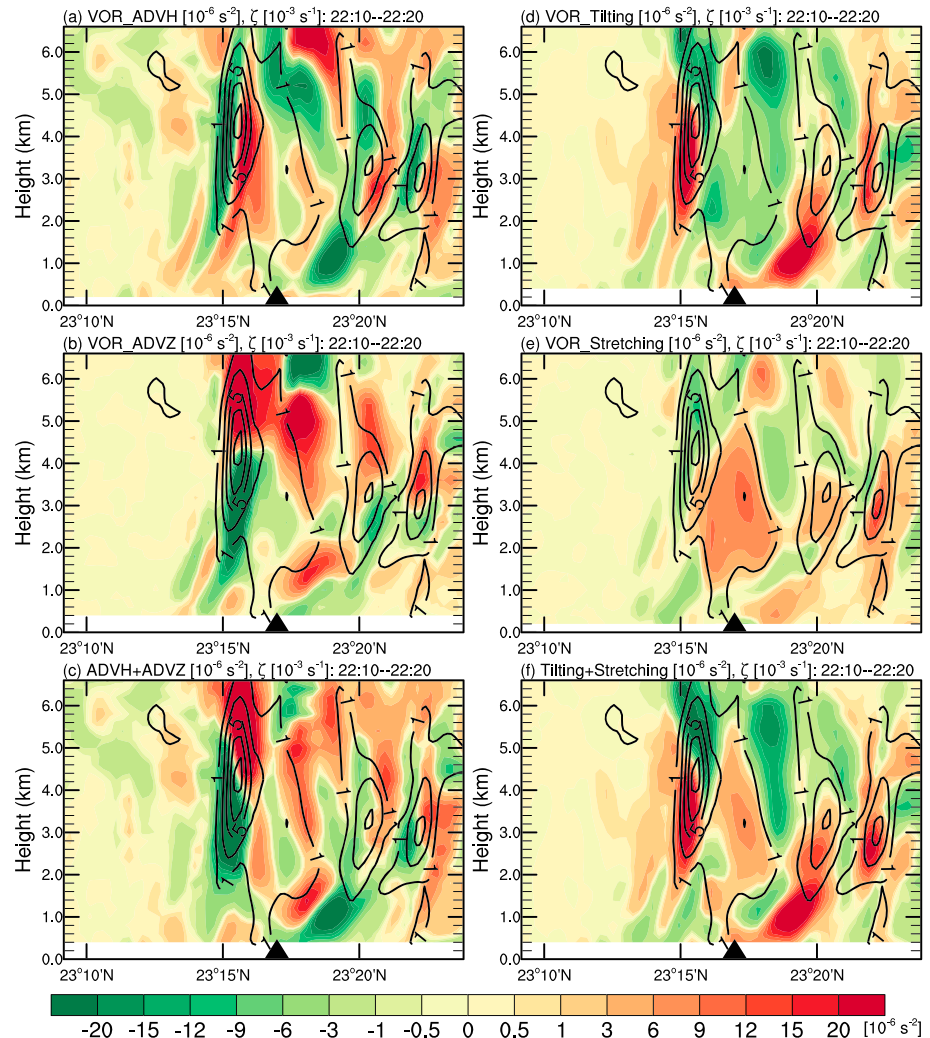
**Figure 8.** Vertical cross sections along the black thick solid lines shown in Figure 5a of time-averaged (2210–2220 UTC 6 May 2017) vertical vorticity tendencies (shaded, $10^{-6}$ s$^{-2}$) due to (a) horizontal advection, (b) vertical advection, (c) total advection, (d) tilting, (e) stretching, and (f) sum of tilting and stretching. The contours in each panel indicate the time-averaged (2210–2220 UTC 6 May 2017) vertical vorticity (1, 3, 5, 7, and $9 \times 10^{-3}$ s$^{-1}$). The black triangles represent the location of maximum accumulated precipitation from 2200 to 2300 UTC 6 May 2017.

Finally, in consideration of the importance of vertical vorticity in NLD_VPPGF, we examine the budget of the vertical vorticity. Figure 8 shows vertical cross sections of the time-averaged (2210–2220 UTC 6 May 2017) vertical vorticity tendencies due to horizontal advection, vertical advection, tilting, stretching, total advection, and the total of tilting and stretching. The solenoid and Coriolis advection are 2 orders of magnitude smaller than these four terms and thus are ignored herein. Besides, the residual term $(\frac{\partial \zeta}{\partial t}_{RES})$ is also small enough to be neglected for the purposes of this study. The horizontal advection mainly moved positive vertical vorticity to the right flank of the maximum vertical vorticity center (Figure 8a). Vertical advection transported the vertical vorticity from lower levels to upper levels (Figure 8b). Tilting was an important source for the development of each vertical vorticity core, and the maximum tilting was mainly located below the maximum vertical vorticity cores (Figure 8d). To obtain a more clear physical picture of the tilting of horizontal vortex tube by updraft, the tilting term $(\frac{\partial w}{\partial y}\frac{\partial u}{\partial z} - \frac{\partial w}{\partial x}\frac{\partial v}{\partial z})$ was examined separately, and the term $\frac{\partial w}{\partial y}\frac{\partial u}{\partial z}$ was found to be the dominant term (not shown). Combining the wind profile and vertical velocity shown in Figure 6, south-northward horizontal vortex tube $(\frac{\partial u}{\partial z})$ was generated and tilted by updrafts/downdrafts. Therefore, there existed positive tilting term on the south flank of updraft and on the north flank of downdraft
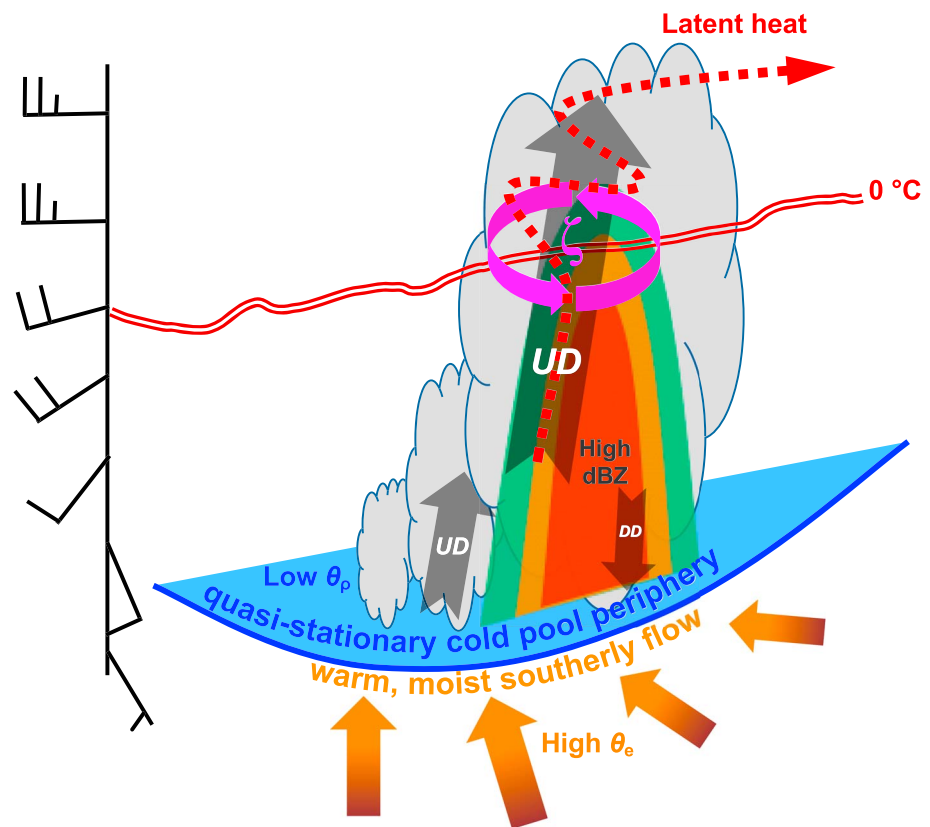
**Figure 9.** Schematic diagram of the mechanisms for this severe rainfall. The wind profile on the left shows the mean horizontal winds (one full wind barb represents 4 m/s). The blue shaded areas and orange arrows on the bottom indicate the cold pool and warm, moist southerly flow, respectively. The gray arrows indicate vertical motions ("UD" for updraft and "DD" for downdraft), the magenta curled arrows show vertical vorticity, and the red dashed winding arrow indicates latent heat removal. The double-solid line represents 0 °C level. The green, orange, and red shaded areas show radar echoes of different intensities.

(Figure 8d). And stretching also made contribution to vertical vorticity development, especially near 3 km (Figure 8e). Thus, strong updrafts enhanced the tilting and stretching of vertical vorticity (Figure 8f), generating strong vertical vorticity and then inducing locally low dynamic perturbation pressure associated with the spin term in equation (8).

## 5. Summary and Conclusions

In this study, budget analyses of water vapor, vertical momentum, potential temperature, and vertical vorticity were presented to investigate the development mechanisms for the record-breaking rainfall in the coastal metropolitan city of Guangzhou, China, during 6–7 May 2017. The budgets were computed based on the model output from a nested very large eddy simulation with the WRF model that reasonably reproduced the heavy rain event (Huang, Liu, et al., 2019). The major findings are summarized as follows.

1.  The main moisture source for the heavy precipitation was the southerly warm, moist onshore flow in the lower troposphere from the South China Sea.
2.  The storm was a quasi-stationary backward propagation MCS, with moderately slantwise strong vertical updrafts that allowed large hydrometeors (low-echo centroid structure) to stay below, and preventing precipitation falling into the lower-level inflow.
3.  The vertical momentum budget analysis indicates that the total buoyancy forcing contributed the most toward supporting development and maintenance of the main updrafts. The warm anomaly air around the main updraft core was transferred downstream by advection, which helped maintain the air parcels' CAPE when lifted in the lower troposphere, and their buoyancy acceleration.

4. The total dynamic acceleration also played a complementary role in supporting the development and maintenance of the main updrafts. The nonlinear dynamic perturbation pressure gradient force in the lower troposphere associated with rotation aloft accelerated the air below the maximum vertical velocity core, helping supply the warm, moist air into the main updrafts.

A conceptual model of the heavy rainfall was developed as Figure 9. The counteraction between the precipitation-produced cold pool outflows and the warm, moist southerly flow (Huang, Liu, et al., 2019) repeatedly triggered new updrafts and convection cells upstream (Figure 4). The vertical environmental wind shear (Figure 3b) caused updrafts to moderate tilt (Figures 3 and 4), preventing the precipitation from falling into the updraft. Sustained abundant warm moisture in the lower troposphere and latent heat removal in the upper troposphere resulted in strong buoyancy forcing for the air parcels in the lower troposphere, which drove the updrafts. The nonlinear dynamic perturbation pressure acceleration associated with rotation by tilting and stretching terms of vertical vorticity generation, and the linear dynamic perturbation pressure acceleration produced by the updrafts interacting with the ambient vertical wind shear forced lower-tropospheric updrafts upstream of the storm. The updrafts were triggered repeatedly and fed convective cells along the quasi-stationary cold pool boundary. The storm was a back-building quasi-stationary MCS, favoring extreme local rainfall. The characteristics of this case are different from the case of Nielsen and Schumacher (2018), in which the dynamical acceleration dominated over buoyant acceleration in the low levels during an extreme rainfall associated with meso-$\beta$-scale vortices that occurred in central Texas in October 2015. There may be many factors causing these differences, such as the supply of low-level moisture in different regions (coastal in this study and inland in their study), the static stability of the environments, the vertical structure of the storms' heating profiles, and the low-level wind shear (direction and strength). These are worth exploring in future.

These results demonstrate the importance of dynamic and thermodynamic factors that affect the precipitation efficiency and vertical moisture flux in forming high precipitation rates when forecasting rare but extreme heavy rainfall (Doswell et al., 1996). In this case, abundant moisture came from the South China Sea in the lower troposphere, buoyancy forcing and dynamic pressure acceleration together supported strong updrafts resulting in strong vertical moisture flux, and low-echo centroid structure was favorable for high precipitation efficiency. All these forcing mechanisms worked together to cause very high precipitation rate and the record-breaking rainfall. Due to the relatively small scale of this precipitation system, subkilometer-scale numerical weather prediction is very important for heavy rainfall forecasts in urban areas.

As mentioned by Huang, Liu, et al. (2019), the combination of the WSM6 microphysical parameterization scheme and the LES mode in the WRF model can sometimes produce better simulations compared to using other double-moment microphysical parameterization schemes and PBL parameterization schemes. In future analyses, we will investigate the cloud microphysical processes and boundary layer processes, partly by executing simulations starting at different initial times using different analysis/forecasts as initial/boundary conditions, and by studying the results' sensitivity to model errors.

## References

Coffer, B. E., & Parker, M. D. (2015). Impacts of increasing low-level shear on supercells during the early evening transition. *Monthly Weather Review*, *143*(5), 1945–1969. https://doi.org/10.1175/MWR-D-14-00328.1

Davies-Jones, R. (2002). Linear and nonlinear propagation of supercell storms. *Journal of the Atmospheric Sciences*, *59*(22), 3178–3205. https://doi.org/10.1175/1520-0469(2003)059<3178:LANPOS>2.0.CO;2

Doswell, C. A. III, Brooks, H. E., & Maddox, R. A. (1996). Flash flood forecasting: An ingredients-based methodology. *Weather and Forecasting*, *11*(4), 560–581. https://doi.org/10.1175/1520-0434(1996)011<0560:FFFAIB>2.0.CO;2

Doswell, C. A. III, & Markowski, P. M. (2004). Is buoyancy a relative quantity? *Monthly Weather Review*, *132*(4), 853–863. https://doi.org/10.1175/1520-0493(2004)132<0853:IBARQ>2.0.CO;2

Fritsch, J. M., & Carbone, R. E. (2004). Improving quantitative precipitation forecasts in the warm season: A USWRP research and development strategy. *Bulletin of the American Meteorological Society*, *85*(7), 955–966. https://doi.org/10.1175/BAMS-85-7-955

Hamada, A., Takayabu, Y. N., Liu, C., & Zipser, E. J. (2015). Weak linkage between the heaviest rainfall and tallest storms. *Nature Communications*, *6*, ncomms7213. https://doi.org/10.1038/ncomms7213

Huang, Y., Liu, Y., Liu, Y., Li, H., & Knievel, J. (2019). Mechanisms for a record-breaking rainfall in the coastal metropolitan city of Guangzhou, China: Observation analysis and nested very-large-eddy simulation with the WRF model. *Journal of Geophysical Research: Atmospheres*, *124*, 1370–1391. https://doi.org/10.1029/2018JD029668

Huang, Y., Liu, Y., Xu, M., Liu, Y., Pan, L., Wang, H., et al. (2018). Forecasting severe convective storms with WRF-based RTFDDA radar data assimilation in Guangdong, China. *Atmospheric Research*, *209*, 131–143. https://doi.org/10.1016/j.atmosres.2018.03.010

Huang, Y., Wang, Y., & Cui, X. (2019). Differences between convective and stratiform precipitation budget processes in a torrential rainfall event. *Advances in Atmospheric Sciences*, *36*(5), 495–509. https://doi.org/10.1007/s00376-019-8159-1

Kermanshah, A., Derrible, S., & Berkelhammer, M. (2017). Using climate models to estimate urban vulnerability to flash floods. *Journal of Applied Meteorology and Climatology*, *56*(9), 2637–2650. https://doi.org/10.1175/JAMC-D-17-0083.1

Klemp, J. B. (1987). Dynamics of tornadic thunderstorms. *Annual Review of Fluid Mechanics*, *19*(1), 369–402. https://doi.org/10.1146/annurev.fl.19.010187.002101

Lamb, D. (2001). Rain production in convective storms. In *Severe Convective Storms* (pp. 299–321). Boston, MA: American Meteorological Society. https://doi.org/10.1007/978-1-935704-06-5_8

Liu, Y., Warner, T. T., Astling, E. G., Bowers, J. F., Davis, C. A., Halvorson, S. F., et al. (2008). The operational mesogamma-scale analysis and forecast system of the US Army test and evaluation command. Part II: Interrange comparison of the accuracy of model analyses and forecasts. *Journal of Applied Meteorology and Climatology*, *47*(4), 1093–1104. https://doi.org/10.1175/2007JAMC1654.1

Liu, Y., Warner, T. T., Bowers, J. F., Carson, L. P., Chen, F., Clough, C. A., et al. (2008). The operational mesogamma-scale analysis and forecast system of the US Army Test and Evaluation Command. Part I: Overview of the modeling system, the forecast products, and how the products are used. *Journal of Applied Meteorology and Climatology*, *47*(4), 1077–1092. https://doi.org/10.1175/2007JAMC1653.1

Luo, Y., & Chen, Y. (2015). Investigation of the predictability and physical mechanisms of an extreme-rainfall-producing mesoscale convective system along the Meiyu front in East China: An ensemble approach. *Journal of Geophysical Research: Atmospheres*, *120*, 10,593–10,618. https://doi.org/10.1002/2015JD023584

Luo, Y., Gong, Y., & Zhang, D. L. (2014). Initiation and organizational modes of an extreme-rain-producing mesoscale convective system along a Mei-Yu Front in East China. *Monthly Weather Review*, *142*(1), 203–221. https://doi.org/10.1175/MWR-D-13-00111.1

Market, P., Allen, S., Scofield, R., Kuligowski, R., & Gruber, A. (2003). Precipitation efficiency of warm-season Midwestern mesoscale convective systems. *Weather and Forecasting*, *18*(6), 1273–1285. https://doi.org/10.1175/1520-0434(2003)018<1273:PEOWMM>2.0.CO;2

Markowski, P., & Richardson, Y. (2010). *Mesoscale meteorology in midlatitudes*. West Sussex, U.K.: John Wiley & Sons. https://doi.org/10.1002/9780470682104

Nielsen, E. R., & Schumacher, R. S. (2018). Dynamical insights into extreme short-term precipitation associated with supercells and mesovortices. *Journal of the Atmospheric Sciences*, *75*(9), 2983–3009. https://doi.org/10.1175/JAS-D-17-0385.1

Parker, M. D., & Johnson, R. H. (2004). Structures and dynamics of quasi-2D mesoscale convective systems. *Journal of the Atmospheric Sciences*, *61*(5), 545–567. https://doi.org/10.1175/1520-0469(2004)061<0545:SADOQM>2.0.CO;2

Peters, J. M., & Schumacher, R. S. (2015). Mechanisms for organization and echo training in a flash-flood-producing mesoscale convective system. *Monthly Weather Review*, *143*(4), 1058–1085. https://doi.org/10.1175/MWR-D-14-00070.1

Rotunno, R., & Klemp, J. B. (1982). The influence of the shear-induced pressure gradient on thunderstorm motion. *Monthly Weather Review*, *110*(2), 136–151. https://doi.org/10.1175/1520-0493(1982)110<0136:TIOTSI>2.0.CO;2

Schumacher, R. S. (2015). Sensitivity of precipitation accumulation in elevated convective systems to small changes in low-level moisture. *Journal of the Atmospheric Sciences*, *72*(6), 2507–2524. https://doi.org/10.1175/JAS-D-14-0389.1

Schumacher, R. S., & Johnson, R. H. (2005). Organization and environmental properties of extreme-rain-producing mesoscale convective systems. *Monthly Weather Review*, *133*(4), 961–976. https://doi.org/10.1175/MWR2899.1

Schumacher, R. S., & Johnson, R. H. (2006). Characteristics of US extreme rain events during 1999–2003. *Weather and Forecasting*, *21*(1), 69–85. https://doi.org/10.1175/WAF900.1

Schumacher, R. S., & Johnson, R. H. (2008). Mesoscale processes contributing to extreme rainfall in a midlatitude warm-season flash flood. *Monthly Weather Review*, *136*(10), 3964–3986. https://doi.org/10.1175/2008MWR2471.1

Schumacher, R. S., & Johnson, R. H. (2009). Quasi-stationary, extreme-rain-producing convective systems associated with midlevel cyclonic circulations. *Weather and Forecasting*, *24*(2), 555–574. https://doi.org/10.1175/2008WAF2222173.1

Schumacher, R. S., & Peters, J. M. (2017). Near-surface thermodynamic sensitivities in simulated extreme-rain-producing mesoscale convective systems. *Monthly Weather Review*, *145*(6), 2177–2200. https://doi.org/10.1175/MWR-D-16-0255.1

Sharif, H. O., Yates, D., Roberts, R., & Mueller, C. (2006). The use of an automated nowcasting system to forecast flash floods in an urban watershed. *Journal of Hydrometeorology*, *7*(1), 190–202. https://doi.org/10.1175/JHM482.1

Smith, J. A., Baeck, M. L., Morrison, J. E., & Sturdevant-Rees, P. (2000). Catastrophic rainfall and flooding in Texas. *Journal of Hydrometeorology*, *1*(1), 5–25. https://doi.org/10.1175/1525-7541(2000)001<0005:CRAFIT>2.0.CO;2

Smith, J. A., Baeck, M. L., Zhang, Y., & Doswell, C. A. III (2001). Extreme rainfall and flooding from supercell thunderstorms. *Journal of Hydrometeorology*, *2*(5), 469–489. https://doi.org/10.1175/1525-7541(2001)002<0469:ERAFFS>2.0.CO;2

Stevenson, S. N., & Schumacher, R. S. (2014). A 10-year survey of extreme rainfall events in the central and eastern United States using gridded multisensor precipitation analyses. *Monthly Weather Review*, *142*(9), 3147–3162. https://doi.org/10.1175/MWR-D-13-00345.1

Vitale, J. D., & Ryan, T. (2013). Operational recognition of high precipitation efficiency and low-echo-centroid convection. *Journal of Operational Meteorology*, *1*(12), 128–143. https://doi.org/10.15191/nwajom.2013.0112

Wang, C. C., Chiou, B. K., Chen, G. T. J., Kuo, H. C., & Liu, C. H. (2016). A numerical study of back-building process in a quasistationary rainband with extreme rainfall over northern Taiwan during 11-12 June 2012. *Atmospheric Chemistry & Physics*, *16*(18), 12359–12382. https://doi.org/10.5194/acp-16-12359-2016

Wang, H., Luo, Y., & Jou, B. J. D. (2014). Initiation, maintenance, and properties of convection in an extreme rainfall event during SCMREX: Observational analysis. *Journal of Geophysical Research: Atmospheres*, *119*, 13,206–13,232. https://doi.org/10.1002/2014JD022339

Weisman, M. L., & Rotunno, R. (2000). The use of vertical wind shear versus helicity in interpreting supercell dynamics. *Journal of the Atmospheric Sciences*, *57*(9), 1452–1472. https://doi.org/10.1175/1520-0469(2000)057<1452:TUOVWS>2.0.CO;2

Zhang, M., & Zhang, D. L. (2012). Subkilometer simulation of a torrential-rain-producing mesoscale convective system in East China. Part I: Model verification and convective organization. *Monthly Weather Review*, *140*(1), 184–201. https://doi.org/10.1175/MWR-D-11-00029.1